Encapsulating Atomic Molybdenum into Hierarchical Nitrogen-doped Carbon Nanoboxes for Efficient Oxygen Reduction

Fei-Xiang Ma[a,c,†] Guobin Zhang[c,†] Meiyu Wang[d,†] Xiongyi Liang[b], Fucong Lyu[c], Xufen Xiao[b], Peng Wang[d, e], Liang Zhen[a], Jian Lu[c], Lirong Zheng[f,*], Yang Yang Li[b,*], and Cheng-Yan Xu[a, *]

[a] Sauvage Laboratory for Smart Materials, School of Materials Science and Engineering, Harbin Institute of Technology (Shenzhen), Shenzhen 518055, China

[b] Department of Materials Science and Engineering, City University of Hong Kong, Kowloon, Hong Kong, China

[c] Department of Mechanical Engineering, City University of Hong Kong, Kowloon, Hong Kong, China

[d] National Laboratory of Solid State Microstructures, College of Engineering and Applied Sciences, Collaborative Innovation Center of Advanced Microstructures and Center for the Microstructures of Quantum Materials, Nanjing University, Nanjing 210093, China

[e] Department of Physics, University of Warwick, Coventry CV4 7AL, UK

[f] Beijing Synchrotron Radiation Facility, Institute of High Energy Physics, Chinese Academy of Sciences, Beijing 100049, China

† These authors contribute equally to this work.

*Corresponding authors: cy_xu@hit.edu.cn (C.-Y. Xu); yangli@cityu.edu.hk (Y. Y. Li); zhenglr@ihep.ac.cn (L. R. Zheng).

Abstract

Construction of single-atom catalysts (SACs) with maximally exposed active sites remains a challenging task mainly because of the lack of suitable host matrices. In this study, hierarchical N-doped carbon nanoboxes composed of ultrathin nanosheets with dispersed atomic Mo (denoted as hierarchical SA-Mo-C nanoboxes) were fabricated *via* a template-engaged multistep synthesis process. Comprehensive characterizations, including X-ray absorption fine structure analysis, reveal the formation of Mo-N_4 atomic sites uniformly anchored on the hierarchical carbon nanoboxes. The prepared catalysts offer structural and morphological advantages, including ultrathin nanosheet units, unique hollow structures and abundant active Mo-N_4 species, that result in excellent activity with a half-wave potential of 0.86 V vs. RHE

and superb stability for the oxygen reduction reaction in 0.1 M KOH; thus, the catalysts are promising air-cathode catalysts for Zn-air batteries with a high peak power density of 157.6 mW cm^{-2}.

Keywords: single-atom catalysts (SACs), Mo-N_4, hollow structures, nanosheets, oxygen reduction reaction

1. Introduction

The high catalytic activity and ultimate atom utilization of single atomic catalysts (SACs) have facilitated enormous progress in both synthesis methodologies and applications in the past few years.[1-5] The oxygen reduction reaction (ORR) is an important application of SACs that has attracted considerable attention because of its crucial role in fuel cells and Zn-air batteries (ZABs).[6-9] Pt-based materials are generally considered to be the most efficient ORR electrocatalysts.[10] However, the high cost and scarcity of the noble metal Pt severely restricts practical applications of these materials. Consequently identifying and designing efficient, low-cost and stable SACs for ORRs has become a pressing objective. To date, considerable effort has been devoted to developing carbon catalysts codoped with transition metals and nitrogen (denoted as M-N-C, where M represents Co, Fe, Cu or/and Mn, *etc*.) that exhibit promising ORR performance.[11-16] Both theoretical calculations and experimental observations have shown that the unprecedented ORR activity of these novel carbon-supported catalysts, principally originates from atomically dispersed nitrogen-coordinated metal sites.[17-24] Although considerable progress has been made in research on M-N-C-based ORR catalysts using nonprecious 3*d* transition metals (including Co, Fe, Cu and Mn, expanding the group of M-N-C-based ORR catalysts to include other nonprecious transition metals, such as the 4*d* metal Mo, remains an urgent task.

Similar to most carbon-supported SACs (e.g., those based on Co, Ni and Fe), isolated Mo atoms can also be anchored on a conductive carbon matrix with the assistance of nitrogen atoms, and the resultant materials have been utilized as diverse electrocatalysts.[25-28] For example, SiO_2 nanospheres were employed as a hard template to disperse atomic Mo on N-doped carbon nanowalls, and the resulting material exhibited excellent electrocatalytic performance for the hydrogen evolution reaction in alkaline solution.[26] Wang and coworkers successfully fabricated a unique Mo single-atom catalyst consisting of oxygen and nitrogen co-coordinated Mo species anchored on porous carbon, which exhibited efficient ORR performance in alkaline media.[28] However, the lack of adequate diffusion channels in most atomic-metal-supported carbon matrices results in the blockage of a considerable portion of the active sites (e.g., metal-N_x moieties), creating "dead zones" during surface catalytic reactions and deteriorating the electrocatalytic performance.[29-31] Alternatively, hierarchical hollow structures created using ultrathin two-dimensional nanosheet units offer intrinsic advantages for supporting metal single atoms, such as open three-dimensional architectures and robust structural stability.[32-34] More importantly, the presence of ultrathin nanosheet subunits considerably shortens the transport routes and exposes an abundance of single-atom active sites.[35] Currently, a library of hierarchical structures with two-dimensional (2D) nanosheet subunits, including Mo_2C nanotubes[36], Fe_3O_4 hollow spheres[37], $NiCo_2O_4$ tetragonal microtubes[38], In_2S_3-$CdIn_2S_4$ nanotubes[39], *etc.*, have been successfully designed and synthesized for diverse electrochemical applications. However, the synthesis of hierarchical carbon hollow structures with 2D nanosheet subunits remains difficult, mainly because of the lack of a suitable carbon precursor.[40] Therefore, it is highly desirable, yet very challenging, to develop metal-single-atom-supported carbon with 3D open architectures that can fully expose catalytically active sites.

In this study, novel hierarchical N-doped carbon nanoboxes composed of ultrathin nanosheets with dispersed atomic Mo (denoted hierarchical SA-Mo-C nanoboxes) were fabricated through a unique template-engaged multistep synthesis process. The catalytically active single-metal Mo-N_x moieties were identified by scanning transmission electron microscopy (STEM) and extended X-ray absorption fine structure (EXAFS) analysis. The unique structural merits and highly dispersed Mo-N_4 active sites enabled the resultant hierarchical SA-Mo-C carbon nanoboxes to exhibit superior ORR performance in 0.1 M KOH, in terms of both activity and durability, to that of commercial Pt/C catalysts, such that the prepared SA-Mo-C nanoboxes can be applied as air-cathode catalysts for ZABs.

2. Experimental section

2.1 Materials

$FeCl_3 \cdot 6H_2O$, NaOH, $(NH_4)_6Mo_7O_{24} \cdot 4H_2O$, dicyandiamide and $NH_3 \cdot H_2O$ were purchased from Sinopharm Chemical Reagent Co., Ltd. Dopamine hydrochloride was purchased from J&K Scientific Ltd. All the chemicals used were received without any purification.

2.2 Synthesis of Fe_2O_3 nanocubes

Highly uniform Fe_2O_3 nanocubes with average size of 630 nm were synthesized based on the previous literature with minor modification.[41] 50 mL of 5.4 M NaOH solution was added to 50 mL of 2.0 M $FeCl_3$ solution within 5 min under vigorous stirring at 75 °C. The light red $Fe(OH)_3$ gel was further stirred for 5 min, and was then aged at 102 °C in a preheated oven for 4 days. For the synthesis of Fe_2O_3 nanocubes with 500 nm and 800 nm, the reaction temperature was set at 100 ºC and 105 ºC, respectively.

2.3 Synthesis of Mo-polydopamine hybrid nanosheets on Fe_2O_3 nanocubes

In a typical synthesis of Mo-polydopamine hybrid nanosheets coated on Fe_2O_3 nanocubes, 400 mg of the as-prepared Fe_2O_3 nanocubes with a size of 650 nm were added into 40 ml of deionized H_2O in a 250 ml glass bottle. After ultrasonic dispersion for 15 min to disperse Fe_2O_3 nanocubes homogeneously, 100 mg of $(NH_4)_6Mo_7O_{24}\cdot 4H_2O$ and 100 mg of dopamine hydrochloride was dissolved into the above solution completely to form Mo-dopamine complex. Then 80 ml of ethanol was poured into the above solution. After stirring for another 5 min, 0.6 ml of 28~30 % $NH_3\cdot H_2O$ was fast added into the above reaction solution and the mixed solution reacted for 60 min at ambient condition with gently stirring. Finally, the red precipitate was harvested by centrifugation, washed with several times with ethanol and dried in vacuum at room temperature for further treatment.

2.4 Synthesis of SA-Mo-C nanoboxes

The as-prepared Mo-polydopamine hybrid nanosheets on Fe_2O_3 nanocubes were first annealed at 500 ^oC in Ar gas flow for 2 h with a fast ramping rate of 10 ^oC/min. The annealed product was then dispersed in 6 M HCl for 24 h to completely remove the Fe_2O_3 cores. And partly Mo content in carbon nanosheets was also removed because of the high concentration of HCl solution. Finally, the black precipitate was harvested by centrifugation, washed with water and ethanol for four times, respectively. To obtain hierarchical SA-Mo-C nanoboxes, 800 mg of dicyandiamide was placed in a boat in a tube upstream of the gas flow, 40 mg of as-obtained carbon nanoboxes was placed in another boat, and the tube furnace was annealed at 900 ^oC in Ar gas flow for 2 h with a moderate heating rate of 5 ^oC/min.

2.5 Characterizations

Scanning electron microscope (SEM) images were observed by using a Philips XL-30 FESEM. The morphology and element distribution of the samples was characterized by a transmission electron microscopy (TEM, JEOL-2100F, 200 kV) equipped with an EDX detector.

X-ray diffraction (XRD) patterns were collected on an X-ray diffractometer (Rigaku) with Cu K_α radiation. The surface chemistry of the samples was analyzed using an X-ray photoelectron spectroscopy (XPS, VG ESCALAB 220i-XL). Raman spectra were measured on a Renishaw 2000 Raman microscope at a laser wavelength of 633 nm. N_2 sorption analysis of the sample were investigated by a Quantachrome Nova 1200e analyzer. The X-ray adsorption fine structure spectra (Mo K-edge) were performed at the 1W1B beamline in the Beijing Synchrotron Radiation Facility (BSRF), China.

2.6 Electrochemical measurements

All the electrochemical measurements were carried out in a three-electrode system at an electrochemical workstation (Pine WD20 Basic) using saturated calomel electrode (SCE) electrode as the reference electrode, carbon rod as the counter electrode and glassy carbon (GC) electrode as the working electrode. For the preparation of well-dispersed catalyst ink, 5 mg of catalyst and 20 μL of Nafion solution (5 wt.%) was first ultrasonically dispersed in 980 uL 9:1 v/v ethanol/water to form a homogeneous solution, then 20 uL of well-dispersed ink was uniformly dropped onto a GC electrode to give a loading mass of 0.50 mg cm^{-2} for all samples including the commercial Pt/C (20%, Sigma). All the measured potentials were referred to reversible hydrogen electrode (RHE) by using the equation: $E_{RHE} = E_{SCE} + 1.009$ V in 0.1 M KOH.

Before electrochemical testing, the fresh 0.1 M KOH solution was saturated with O_2 by bubbling oxygen for 30 min. For the cyclic voltammetry (CV) test, the working electrode was cycled between −1.0 V and 0.2 V vs RHE at 20 mV s^{-1}. Rotating ring-disk electrode (RRDE) and rotating disk electrode (RDE) measurements were carried out on an electrode rotator equipment (Pine Instrument) and the WD20 Basic potentiostation. The transferred electron number (n) was determined by the following Koutechy-Levich (K-L) equation:

$$\frac{1}{J} = \frac{1}{J_{\mathrm{L}}} + \frac{1}{J_{\mathrm{K}}} = \frac{1}{Bw^{1/2}} + \frac{1}{J_{\mathrm{K}}} \quad (1)$$

$$\mathrm{B} = 0.62\ \mathrm{nF}C_0(D_0)^{2/3}v^{-1/6} \quad (2)$$

$$J_K = nFkC_0 \quad (3)$$

where J represents the measured current density, J_{K} and J_{L} are the kinetic and diffusion limiting current densities, respectively, ω is the electrode rotating rate, F is Faraday constant (96485 C mol^{-1}), C_0 is the bulk concentration of O_2 (1.2×10^{-3} mol cm^{-3}), v is the kinematic viscosity (0.01 $cm^2\ s^{-1}$), and D_0 is the diffusion coefficient of O_2 (1.9×10^{-5} $cm^2\ s^{-1}$).

The n and HO_2^- yield were calculated based on the equation (4) and (5):

$$n = \frac{4I_{disk}}{I_{disk} + \frac{I_{ring}}{N}} \quad (4)$$

$$H_2O_2\% = \frac{200\frac{I_{ring}}{N}}{\frac{I_{ring}}{N} + I_{disk}} \quad (5)$$

where I_{disk} is disk electrode current, I_{ring} is ring electrode current, and N is collection efficiency at the ring electrode and determined to be 0.37.

The long-term durability of SA-Mo-C nanoboxes and the commercial Pt/C catalyst was investigated by accelerated durability test (ADTs) with 5000 cycles between 0.6 and 1.0 V vs. RHE. To evaluate the tolerance towards methanol, chronoamperometric measurements at 0.7 V vs. RHE were performed in a O_2-saturated mixed solution containing 3 M methanol in 0.1 M KOH along.

3. Results and discussion

3.1 Synthesis and characterization of SA-Mo-C nanoboxes

In this study, a unique template-engaged multistep synthesis process was adopted to prepare novel hierarchical SA-Mo-C nanoboxes from ultrathin nanosheets. The overall synthetic process of the hierarchical SA-Mo-C nanoboxes is schematized in **Fig. 1**. First, Mo-polydopamine complex nanosheets that can strongly adhere to various substrates are uniformly coated on pre-synthesized Fe_2O_3 nanocubes to form a unique core-shell architecture. Second, amorphous hierarchical carbon nanoboxes with groups containing trace Mo are formed through low-temperature pyrolysis (~500 °C) and subsequent acid washing. Finally, the isolated Mo atoms are uniformly and firmly packaged in carbon nanosheet subunits through nitrogen trapping after high-temperature calcination in a CN_x-rich atmosphere yielded by cyanamide pyrolysis, resulting in the formation of hierarchical SA-Mo-C carbon nanoboxes.

In a typical experiment, highly uniform Fe_2O_3 nanocubes with an average size of 630 nm (**Figs. 2**a-c and Fig. S1) were first prepared using a hydrothermal reaction and employed as a hard template.[41] Subsequently, self-polymerized Mo-conjugated dopamine nanosheets, with a thickness of 5 nm determined from an AFM image (Fig. S2), were evenly coated on the surface of pre-synthesized Fe_2O_3 nanocubes (Figs. S3 and S4) through a facile liquid-phase reaction process at room temperature. Note that in the absence of an Fe_2O_3 template, uniform flower-like Mo-polydopamine nanospheres with sizes of ca. 200 nm were generated (Fig. S5), indicating the strong adhesion ability of the Mo-polydopamine nanosheets. The Mo-polydopamine-coated Fe_2O_3 precursor was then annealed under an inert atmosphere to obtain Fe_3O_4/C-MoO_x core-shell structures (Fig. 2d-f and Fig. S6). The *in situ* and confined pyrolysis produced ultrasmall MoO_x nanocrystals embedded in the carbon nanosheet matrix.[36, 42] Pickling the resultant nanosheets in 6 M HCl solution removed the Fe_3O_4 core and most of the MoO_x confined in the carbon nanosheet shells to produce hierarchical carbon nanoboxes with a trace number of residual Mo groups (Figs. S7 and S8). Finally, high-temperature

calcination was performed in a CN_x-rich atmosphere to yield the target product, hierarchical SA-Mo-C nanoboxes with abundant Mo-N_x atomic sites dispersed on the nanosheet subunits. Without the addition of an MoO_4^{2-} source, uniform carbon nanoboxes with smooth surfaces (Fig. S9) were generated.

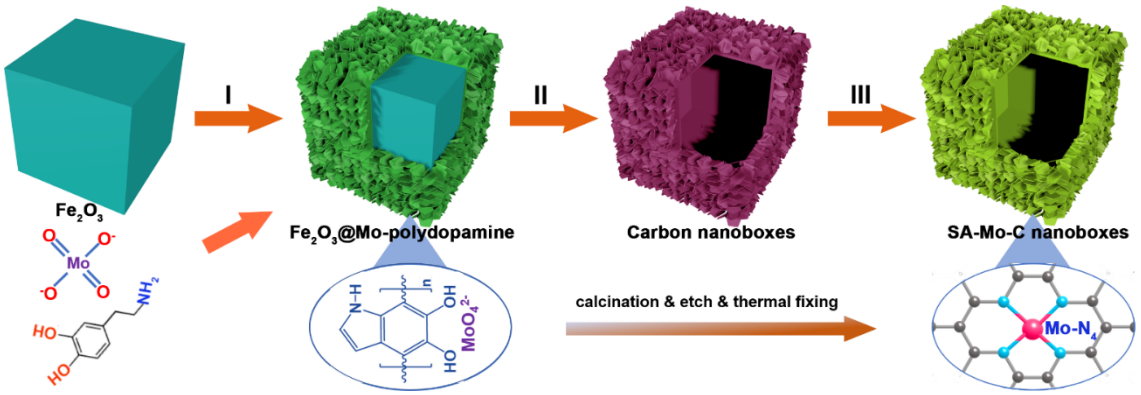

Fig. 1. Schematic depiction of the fabrication process of hierarchical SA-Mo-C nanoboxes. (I) fabricating Fe_2O_3@Mo-polydopamine through a solution reaction, (II) obtaining carbon nanoboxes with a trace of residual Mo groups through subsequent annealing and acid washing, (III) generating SA-Mo-C nanoboxes after high-temperature calcination.

The low-magnification FE-SEM image in Fig. 2g shows highly dispersed nanoboxes without any adhesion and perfectly inherited cubic shapes with an average size of approximately 800 nm (Fig. S10). High-magnification FE-SEM images (Fig. 2h) clearly show that the SA-Mo-C nanoboxes are composed of abundant carbon nanosheets that create a rough and open 3D architecture. The hollow interior and geometrical structure of the as-obtained hierarchical SA-Mo-C nanoboxes were further elucidated by transition electron microscopy (TEM). In agreement with the abovementioned FE-SEM findings, inner cavities can be clearly observed by the sharp contrast between the carbon nanosheet shell and hollow interior. The shells of these nanoboxes are uniform and highly porous, with a wall thickness of approximately 80 nm (Fig. 2i). A magnified TEM image of one corner of a single nanobox (Fig. S11a) shows that the shell is constructed of ultrathin nanosheets with a thickness of approximately 4 nm.

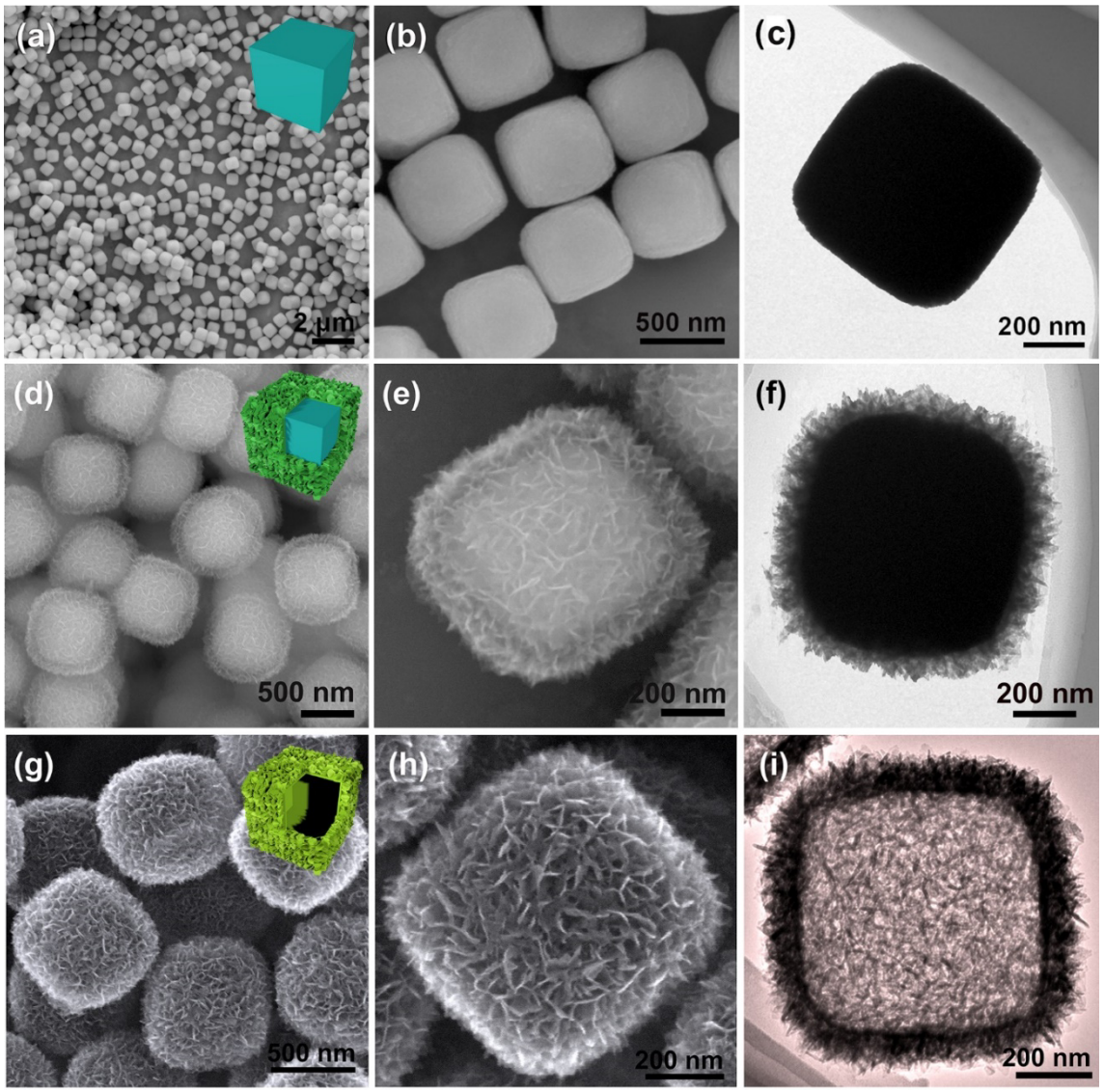

Fig. 2. SEM and TEM images of (a-c) Fe_2O_3 nanocubes, (d-f) Fe_2O_3@MoO_x/C core-shell nanocubes and (g-i) hierarchical SA-Mo-C nanoboxes. The insets in panels a, d and g were the corresponding schematic image.

A high-angle annular dark-field scanning transmission electron microscope (HAADF-STEM) image (**Fig. 3**a) shows a highly porous structure with an open three-dimensional architecture and uniform contrast. A high-magnification TEM image (Fig. 3b) shows that the nanosheet subunits are highly porous with pore sizes of several nanometers. Such tiny pores would have been created by the removal of the MoO_x nanoparticles from the pristine MoO_x/C nanosheets. The high-resolution TEM (HRTEM) image in Fig. 3c shows that the lattice spacing of the carbon nanosheets is approximately 0.38 nm (inset of Fig. 3c), which is slightly higher than that of the interfacial layer of graphitized carbon.

The aberration-corrected HAADF-STEM image (Fig. 3d) reveals a considerable number of bright dots on a single nanosheet subunit, indicating a dense and even distribution of isolated Mo atoms. EDS elemental maps (Fig. 3e) confirm that elemental N, C and Mo are uniformly distributed throughout the entire nanobox. The ICP–OES results show an Mo content in the hierarchical SA-Mo-C nanoboxes of approximately 4.5 wt.%, which is considerably higher than that of most previously reported carbon-substrate-supported SACs. The ring-like selected-area electron diffraction (SAED) patterns shown in Fig. S11b imply low crystallinity for the SA-Mo-C nanoboxes. Notably, Fe_2O_3 nanocubes of different sizes (500 and 850 nm) can be used as removable templates to tune the particle size of the hierarchical SA-Mo-C nanoboxes from 650 nm to 1 μm (Figs. S12 and S13). The as-prepared hierarchical SA-Mo-C nanoboxes exhibit a high surface area of 241.2 $m^2\ g^{-1}$ (Fig. 3f). A plot of the Barrett–Joyner–Halenda (BJH) pore-diameter distribution (inset of Fig. 3f) reveals that the hierarchical SA-Mo-C nanoboxes possess a bimodal pore size distribution centered at ~4 and ~13 nm, where both sizes indicate a mesoporous structure.

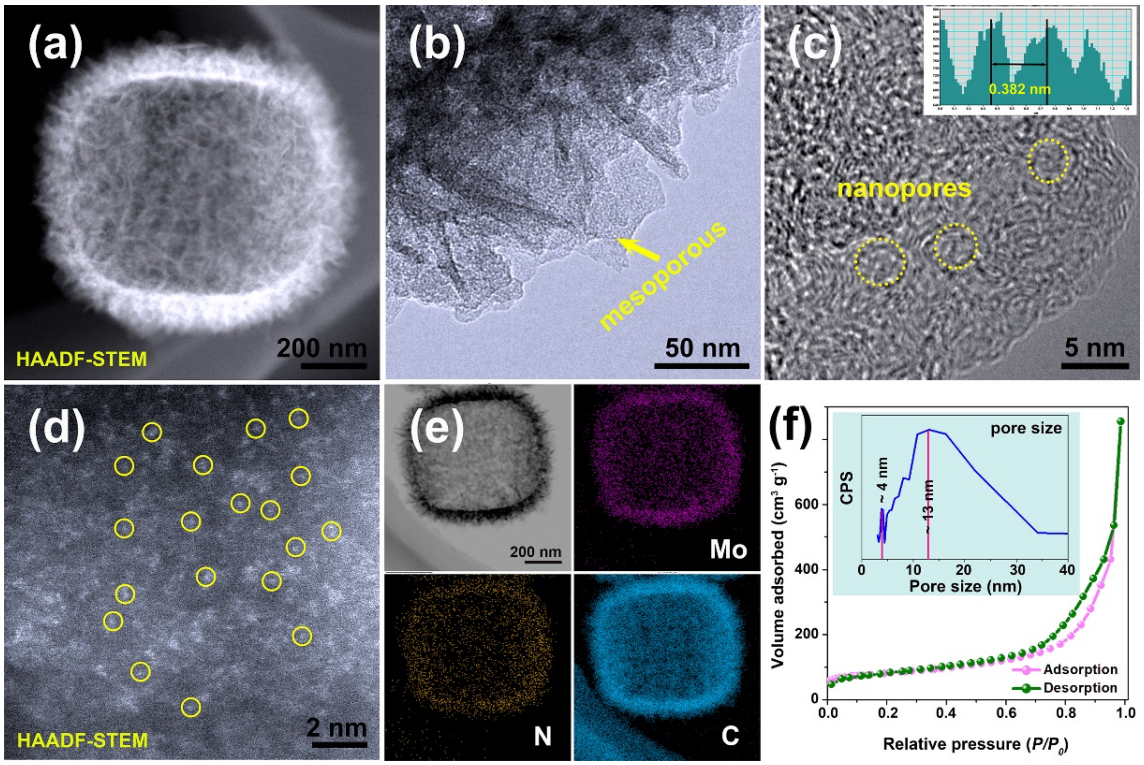

Fig. 3. Morphology and atomic structure of hierarchical SA-Mo-C nanoboxes. (a) Representative STEM image of a single nanobox; (b, c) HRTEM images of the nanosheet subunits. Inset in (c) was the contrast intensity profile of the lattice fringes; (d) atomic-resolution HAADF-STEM image, yellow circles in (d) denote isolated Mo atoms; (e) elemental mapping images of Mo, N and C elements; (f) N_2 adsorption-desorption isotherms. Inset in (f) is BJH method-based pore size distribution.

The valence state and coordination condition of the Mo species in the SA-Mo-C nanoboxes were investigated by Mo K-edge XANES and EXAFS spectroscopy using Mo, MoO_2 and MoO_3 as reference samples. The absorption edge of SA-Mo-C is located between that of Mo and MoO_2 (**Fig. 4**a), demonstrating that the valence of the Mo species in the SA-Mo-C nanoboxes is below +4. This low oxidation valence of Mo should be ascribed to carbon thermal reduction at high temperature. The Fourier-transformed (FT) EXAFS spectra of the SA-Mo-C nanoboxes and the relevant reference samples are shown in Fig. 4b. The predominant FT peak at ~1.13 Å in the spectrum of the SA-Mo-C nanoboxes can be assigned to the Mo-N/O scattering path. Moreover, WT contour plots of Mo, MoO_2 and MoO_3 show Mo-Mo paths at ~2.3, ~3.24 and ~3.37 Å, respectively, whereas no appreciable Mo-Mo path is observed for SA-Mo-C. Combining the STEM observation with the FT EXAFS results reveal that the Mo atoms in SA-Mo-C nanoboxes are apparently isolated from each other.[25, 27] To further determine the coordination conditions of the Mo species in the SA-Mo-C nanoboxes, wavelet transform (WT) analysis was used to supplement EXAFS in energy space (Fig. 4c). The WT contour plots for the SA-Mo-C sample exhibit one dispersed maximum in the intensity in *k*-space at ~7.1 $Å^{-1}$, which is assigned to the Mo-N path. Unlike the WT paths for Mo, MoO_2 and MoO_3 (Fig. S14), no WT signals related to Mo-Mo coordination were detected, further demonstrating the presence of Mo single atoms in the hierarchical carbon nanoboxes. An EXAFS fitting analysis (Fig. 4d) provided the coordination number and bonding distance of the central Mo atoms with respect to the neighboring scattering atoms in SA-Mo-C, providing a first-shell Mo-N coordination number and

bonding distance of ~4.2 and ~1.13 Å, respectively. These results confirmed that the single Mo atom in SA-Mo-C was configured as Mo-N_4, that is, the central Mo atom was coordinated with four nitrogen atoms (inset in Fig. 4d). The XRD pattern of the hierarchical SA-Mo-C nanoboxes (Fig. S15a) shows that there are only two typical diffraction peaks located at approximately 24° and 44°, corresponding to the (002) and (100) crystallographic planes of graphite, respectively.[43] This result is highly consistent with the abovementioned SAED result. The electronic structure of the sample was further investigated by Raman spectroscopy and X-ray photoelectron spectroscopy (XPS). The Raman spectra in Fig. S15b display characteristic D and G bands at 1336 and 1584 cm^{-1}, respectively, which can be assigned to disordered and graphitic carbon atoms, respectively.[44, 45] The high I_D/I_G ratio (up to 1.12) can be ascribed to the distortion of the carbon structure and defects induced by Mo and N codoping. In general, the structural defects can significantly enhance chemical adsorption of oxygen on the catalyst surface and endow carbons with more catalytic active sites for the ORR.[46, 47] The XPS survey curve in Fig. S16 shows the presence of elemental Mo, N and C in the SA-Mo-C nanoboxes. The high-resolution XPS spectra of Mo 3d (Fig. 4e) can be perfectly fitted by two peaks, where the binding energies at 235.0 and 231.9 eV correspond to Mo $3d_{3/2}$ and Mo $3d_{5/2}$, respectively. These energy values are slightly low compared to previously reported values for Mo^{4+}, which strongly suggests that the valence of Mo in SA-Mo-C nanoboxes is < +4, consistent with the XANES results.[28, 48] In the XPS spectrum for N 1s, the peaks at 398.9, 400.3, and 401.2 eV reveal the presence of pyridinic, pyrrolic, and graphitic N, respectively, whereas the intense peak at 307.7 eV can be ascribed to the Mo-N bonds (Fig. 4f). Based on the comprehensive analysis presented above, the atomically dispersed Mo atoms most likely form Mo-N_4 speciation in the N-doped carbon matrix, similar to other M-N-C catalysts.

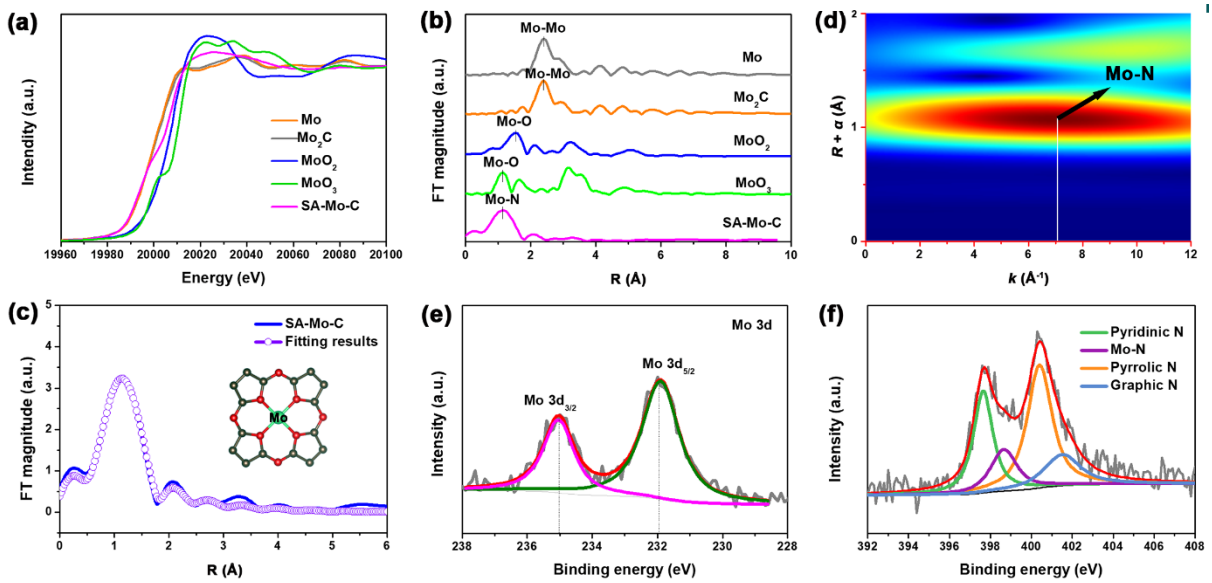

Fig. 4. XAS and XPS characterization of SA-Mo-C nanoboxes. (a) Mo K-edge XANES spectra and (b) k^3-weighted FT EXAFS spectra of the SA-Mo-C and references samples (MoO_2, MoO_3 and Mo foil). (c) k^3-weighted WT EXAFS spectra and (d) EXAFS fitting curve of SA-Mo-C. High-resolution XPS spectra for (e) Mo 3d and (f) N 1s. The inset in (d) was the atomic structure model of SA-Mo-C).

3.2 Electrochemical performance

The results of electrochemical experiments demonstrated that the ORR performance of hierarchical SA-Mo-C nanoboxes surpasses that of commercial Pt/C in terms of both activity and durability. To quantify the ORR activity, polarization curves were measured by RDE technology. The hierarchical SA-Mo-C nanoboxes were optimized for use as ORR catalysts at different calcination temperatures, and polarization curves showed that the sample prepared at 900 °C (denoted as SA-Mo-C900) exhibited the highest ORR activity. CV measurements (**Fig. 5**a) show that the cathodic peak for oxygen reduction by the SA-Mo-C nanoboxes occurs at 0.82 V vs. RHE. The results of LSV tests presented in Fig. 5b show that the SA-Mo-C900 sample has the highest half-wave potential ($E_{1/2}$) of 0.86 V vs. RHE, which is as much as 30 mV more positive than that of commercial Pt/C. The mass activity of the SA-Mo-C nanoboxes at 0.85 V vs. RHE is 5.6 times higher

than that of Pt/C (Fig. S17), illustrating the high Mo utilization of the nanoboxes. In addition, the $E_{1/2}$ values of SA-Mo-C800 and SA-Mo-C1000 are 0.82 V and 0.79 V vs. RHE, respectively, indicating that the calcination temperature affects the ORR properties. Furthermore, the inferior ORR performance of the carbon nanoboxes without the addition of the MoO_4^{2-} source and SA-Mo-C nanoflowers (Fig. S18) confirms that both the Mo-N_4 moieties and hierarchical hollow structures make critical contributions to the excellent ORR activity of the SA-Mo-C nanoboxes. The ICP–OES results show that the Fe content of the hierarchical SA-Mo-C nanoboxes is negligible (< 0.01 wt.%), verifying that the remarkable catalytic activity originates from the dense Mo-N_4 active sites rather than the very dilute Fe-N_x moieties. Compared to the other three samples, SA-Mo-C900 delivers a higher diffusion-limited current density of ca. 6.0 mA cm^{-2}, indicating that the hierarchical nanoboxes possess abundant accessible active sites that boost the ORR. Tafel plots (Fig. 5c) were used to examine the specific activity-potential relationship. The Tafael slope of SA-Mo-C900 of 47 mV dec^{-1} is considerably lower than those of SA-Mo-C800 (72.3 mV dec^{-1}), SA-Mo-C1000 (70.2 mV dec^{-1}) and even Pt/C (60 mV dec^{-1}). This result indicates faster dynamics for SA-Mo-C900 in the ORR compared to the other samples. The ORR activity of SA-Mo-C900, reflected by both the $E_{1/2}$ and Tafel slopes, is further highlighted in Fig. 5d. RDE measurements were carried out at different rotations to elucidate the ORR pathway of SA-Mo-C900, which is shown in Fig. 5e. The K–L equation was used to calculate a number of electron transfers (n) in the range of 3.88–3.96 over the potential range of 0.3–0.6 V (inset of Fig. 5e), which approaches the theoretical value of 4.00 for a four-electron ORR process. The RDE measurements (Fig. 5f) demonstrate that the SA-Mo-C900 catalyst exhibits a low H_2O_2 yield of below 5% with a large electron-transfer number of 3.9 over the potential range of 0.2–0.9 V, further confirming that the ORR process occurs via a four-electron pathway. Therefore, the ORR catalyzed by SA-Mo-C900 follows a 4-electron pathway,

similar to that of commercial Pt/C-based catalysts. As the durability of catalysts is another significant criterion for practical applications, the hierarchical SA-Mo-C nanoboxes were further subjected to accelerated durability tests (ADTs) and chronoamperometry measurements for stability evaluation. The LSV curve of the SA-Mo-C nanoboxes after 5000 cycles of ADTs shows only a 1-mV decline in $E_{1/2}$ (Fig. 5g), which is considerably smaller than that of Pt/C (which shows an 18-mV decline, as presented in Fig. S19). Setting the electrode potential at 0.7 V vs. RHE results in a current loss after 20 h of chronoamperometric testing of < 3% for the SA-Mo-C nanoboxes, whereas the decay is > 30% for Pt/C (Fig. 5h). The SA-Mo-C nanoboxes show significantly better long-term durability in alkaline media than Pt/C. Furthermore, the SA-Mo-C nanoboxes possess a superior tolerance toward methanol, with a negligible current loss after the injection of 3 mL of methanol compared to a current loss of up to 19% for Pt/C (Fig. 5i).

The outstanding ORR performance of the hierarchical SA-Mo-C nanoboxes in alkaline media can be ascribed to unique structural and compositional advantages. These advantages are as follows: (1) the unique hierarchical nanoboxes with a 3D open framework facilitate fast mass transport of reactants and electron transfer. (2) The ultrathin nanosheet subunits enable complete exposure of the active components, typically including unique Mo-N_4 active sites. (3) The abundant exposed atomic Mo-N_4 sites may improve the adsorption strength for O_2 and decrease the formation energy of oxygen-containing intermediates, thereby boosting the ORR activity of the SA-Mo-C nanoboxes. (4) The high fraction of doped graphitic-N and pyridinic-N in the carbonaceous matrix induce alternation of the C electronic structure, which could facilitate oxygen adsorption and thereby significantly accelerate the reaction step in the ORR process.

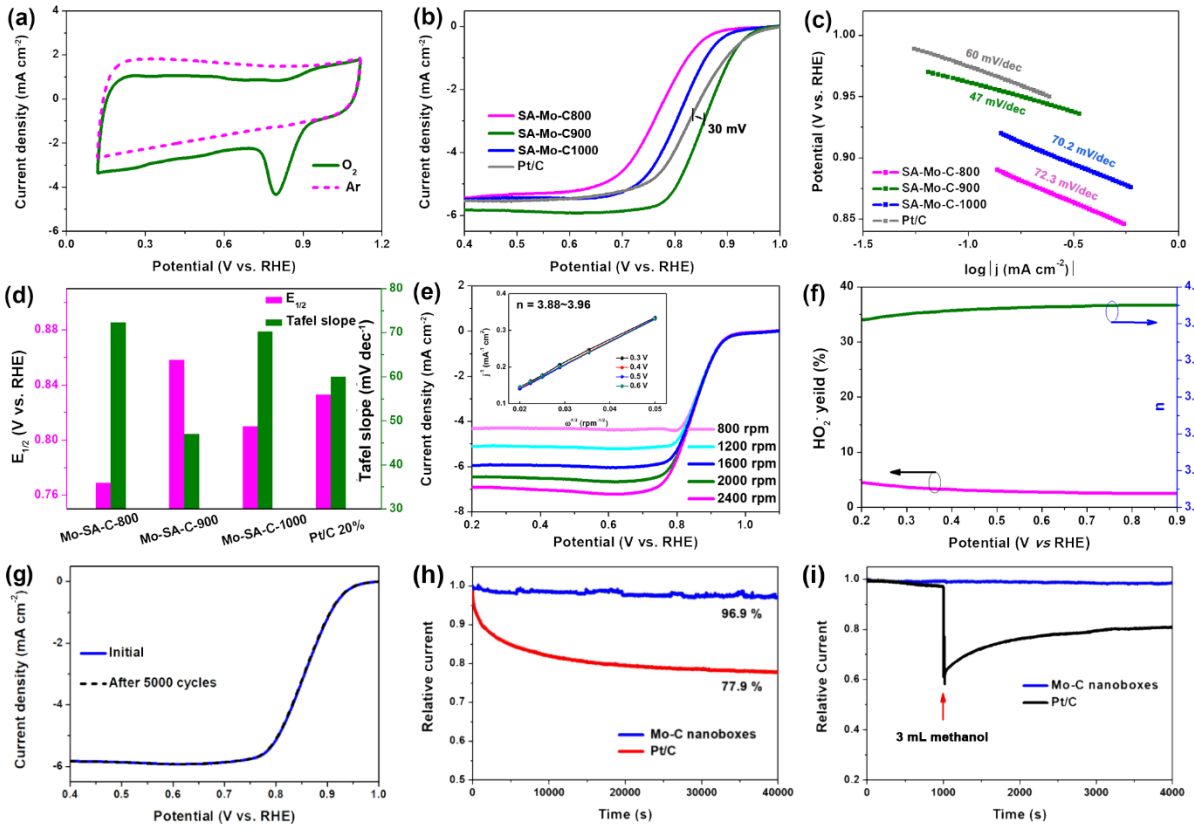

Fig. 5. ORR catalysis properties of hierarchical SA-Mo-C nanoboxes in 0.1 M KOH solution. (a) CV curves at a scan rate of 20 mV s^{-1} in O_2 and Ar saturated solution, (b) LSV curves of samples obtained at different calcination temperatures and commercial 20% Pt/C (1600 rpm, 5 mV s^{-1}), (c) Tafel plots obtained at different calcination temperatures and commercial 20% Pt/C, (d) $E_{1/2}$ and Tafel slopes obtained at different calcination temperatures and commercial 20% Pt/C, (e) The LSV curves at different rotating rates (inset: K-L plots and electron transfer number), (f) H_2O_2 yield and electron transfer number (n) vs. potential, (g) Polarization curves before (solid curves) and after (dashed curves) the accelerated durability tests, (h) chronoamperometric responses by setting the electrode potential at 0.7 V vs RHE and (i) tolerance towards methanol during the chronoamperometric test.

3.3 Electrochemical performance of assembled ZABs

Considering the impressive ORR performance of the SA-Mo-C nanoboxes, the application potential of the nanoboxes to real energy devices was evaluated by assembling ZABs using SA-Mo-C nanoboxes as cathode catalysts (**Fig. 6**). The open-circuit voltage (OCP) of the as-fabricated ZAB can be stabilized at approximately 1.5 V, indicating good practicability for the SA-Mo-C nanoboxes (Fig. 6a). The discharge polarization curve and corresponding peak power density presented in Fig. 6b demonstrate that the peak power density can reach 157.6 mW cm^{-2} at a current density

of 260 mA cm^{-2}, which are comparable to those of ZABs assembled using advanced Fe/Co-N-C catalysts (Table S1).[49-57] The galvanostatic discharge curves at different current densities (2-50 mA cm^{-2}) presented in Fig. 6c demonstrate good rate performance for the ZAB catalyzed by the SA-Mo-C nanoboxes. When discharged at a current density of 20 mA cm^{-2}, the assembled ZAB displays a robust long-term capability without noticeable voltage decay (the loss is only 30 mV after 13 h, Fig. 6d). In summary, all the above-mentioned results demonstrate that the SA-Mo-C nanoboxes not only exhibit a high ORR performance but can also be applied as potential air-cathode catalysts for ZABs.

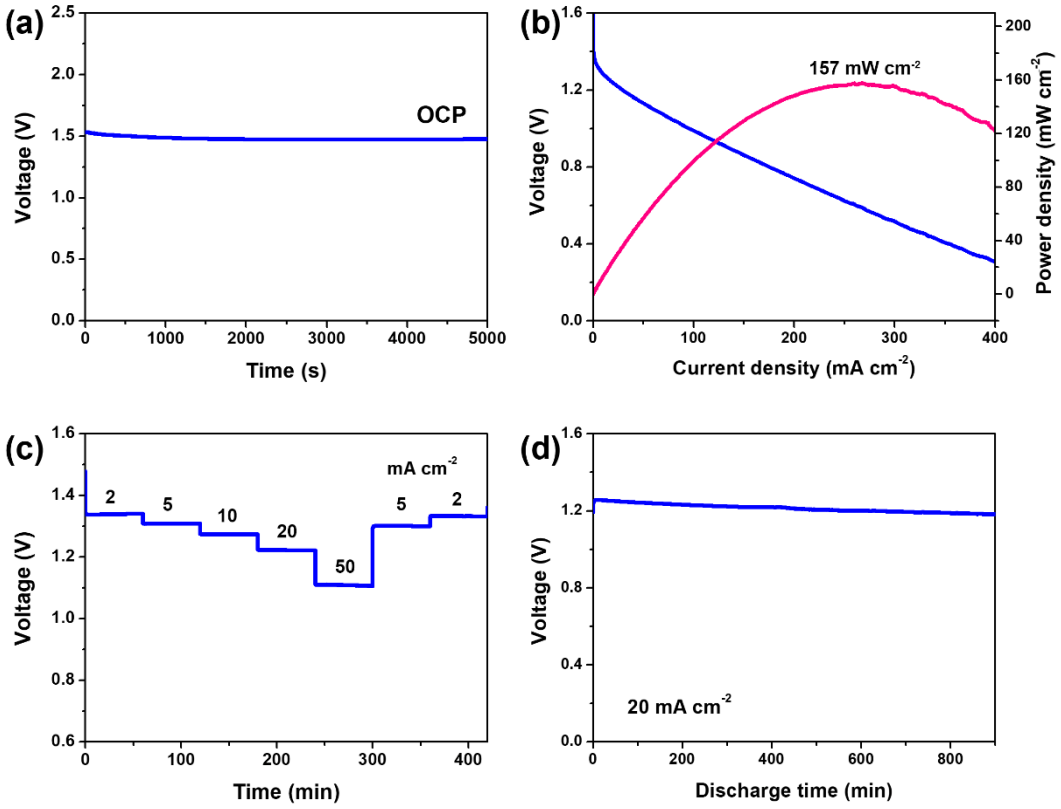

Fig. 6. Performance of ZABs using SA-Mo-C nanoboxes as air cathode catalysts. (a) OCP curve, (b) discharge polarization and power density curves, (c) rating performance at different current density and (d) discharge curve at a current density of 20 mA cm^{-2}.

4. Conclusions

In summary, a unique template-engaged multistep synthesis process was adopted to fabricate hierarchical SA-Mo-C nanoboxes from ultrathin nanosheets with a three-dimensional open architecture to maximally utilize active electrocatalytic sites. Ultrathin nanosheet subunits with dispersed atomic Mo were prepared using a Mo-polydopamine nanosheet precursor. Due to unique hierarchical hollow structures with 3D open architectures, large exposed surface areas, and highly active Mo-N_4 atomic sites, the hierarchical SA-Mo-C nanoboxes demonstrate superior ORR properties to commercial Pt/C under alkaline conditions and are therefore promising air-cathode catalysts for ZABs. The results of this study show that a rational morphology design of SAC-supported carbon substrates can completely expose active sites and ensure sufficient mass transport.

Declaration of Competing Interest

The authors declare that they have no known competing financial interests or personal relationships that could have appeared to influence the work reported in this paper.

Acknowledgements

This work was partially supported by the Innovation and Technology Commission of HKSAR through Project ITS/453/17, Hong Kong Branch of National Precious Metals Material Engineering Research Center, Shenzhen Science and Technology Innovation Committee (JCYJ20200109113212238). J. Lu acknowledges the supports of the National Key R&D Program of China (No. 2017YFA0204403), and the Major Program of National Natural Science Foundation of China (Grant No. 51590892). The authors also thank the Beijing Synchrotron Radiation Facility (BSRF) for the XAFS experiments (1W1B beamline).

[1] Y. Chen, S. Ji, C. Chen, Q. Peng, D. Wang, Y. Li, Single-Atom Catalysts: Synthetic Strategies and Electrochemical Applications, Joule, 2 (2018) 1242-1264.

[2] L. Liu, A. Corma, Metal Catalysts for Heterogeneous Catalysis: From Single Atoms to Nanoclusters and Nanoparticles, Chem. Rev., 118 (2018) 4981-5079.
[3] A. Wang, J. Li, T. Zhang, Heterogeneous single-atom catalysis, Nat. Rev. Chem., 2 (2018) 65-81.
[4] S. Ye, F. Luo, Q. Zhang, P. Zhang, T. Xu, Q. Wang, D. He, L. Guo, Y. Zhang, C. He, X. Ouyang, M. Gu, J. Liu, X. Sun, Highly stable single Pt atomic sites anchored on aniline-stacked graphene for hydrogen evolution reaction, Energy Environ. Sci., 12 (2019) 1000-1007.
[5] Z. Chen, W. Chen, L. Zheng, T. Huang, J. Hu, Y. Lei, Q. Yuan, X. Ren, Y. Li, L. Zhang, S. Huang, S. Ye, Q. Zhang, X. Ouyang, X. Sun, J. Liu, Rational design of Ru species on N-doped graphene promoting water dissociation for boosting hydrogen evolution reaction, Sci. China Chem., 65 (2022) 521-531.
[6] M. Shao, Q. Chang, J.P. Dodelet, R. Chenitz, Recent Advances in Electrocatalysts for Oxygen Reduction Reaction, Chem. Rev., 116 (2016) 3594-3657.
[7] M.K. Debe, Electrocatalyst approaches and challenges for automotive fuel cells, Nature, 486 (2012) 43-51.
[8] P. Wang, Y. Ren, R. Wang, P. Zhang, M. Ding, C. Li, D. Zhao, Z. Qian, Z. Zhang, L. Zhang, L. Yin, Atomically dispersed cobalt catalyst anchored on nitrogen-doped carbon nanosheets for lithium-oxygen batteries, Nat. Commun., 11 (2020) 1576.
[9] Y. Guan, Y. Li, S. Luo, X. Ren, L. Deng, L. Sun, H. Mi, P. Zhang, J. Liu, Rational design of positive-hexagon-shaped two-dimensional ZIF-derived materials as improved bifunctional oxygen electrocatalysts for use as long-lasting rechargeable Zn–Air batteries, Appl. Catal. B: Environ., 256 (2019) 117871.
[10] L. Zhang, K. Doyle-Davis, X. Sun, Pt-Based electrocatalysts with high atom utilization efficiency: from nanostructures to single atoms, Energy Environ. Sci., 12 (2019) 492-517.
[11] U. Martinez, S. Komini Babu, E.F. Holby, H.T. Chung, X. Yin, P. Zelenay, Progress in the Development of Fe-Based PGM-Free Electrocatalysts for the Oxygen Reduction Reaction, Adv. Mater., 31 (2019) e1806545.
[12] Y. Peng, B. Lu, S. Chen, Carbon-Supported Single Atom Catalysts for Electrochemical Energy Conversion and Storage, Adv. Mater., 30 (2018) 1801995.
[13] X. Wang, Z. Li, Y. Qu, T. Yuan, W. Wang, Y. Wu, Y. Li, Review of Metal Catalysts for Oxygen Reduction Reaction: From Nanoscale Engineering to Atomic Design, Chem, 5 (2019) 1486-1511.
[14] Z. Yang, B. Chen, W. Chen, Y. Qu, F. Zhou, C. Zhao, Q. Xu, Q. Zhang, X. Duan, Y. Wu, Directly transforming copper (I) oxide bulk into isolated single-atom copper sites catalyst through gas-transport approach, Nat. Commun., 10 (2019) 3734.
[15] Y. Guo, Z. Wang, Y. Wang, L. Ma, N. Zhang, R. Jiang, Efficient oxygen reduction electrocatalyst derived from facile Fe,N-surface treatment of carbon black, J. Colloid Interface Sci., 605 (2022) 101-109.
[16] Q. Zhao, X. Tan, T. Ma, F. Cao, Z. Xia, H. Liu, H. Ning, Z. Li, H. Hu, M. Wu, Reinforced atomically dispersed FeNC catalysts derived from petroleum asphalt for oxygen reduction reaction, J. Colloid Interface Sci., 587 (2021) 810-819.
[17] Z. Jiang, W. Sun, H. Shang, W. Chen, T. Sun, H. Li, J. Dong, J. Zhou, Z. Li, Y. Wang, R. Cao, R. Sarangi, Z. Yang, D. Wang, J. Zhang, Y. Li, Atomic interface effect of a single atom copper catalyst for enhanced oxygen reduction reactions, Energy Environ. Sci., 12 (2019) 3508-3514.
[18] Z. Lu, B. Wang, Y. Hu, W. Liu, Y. Zhao, R. Yang, Z. Li, J. Luo, B. Chi, Z. Jiang, M. Li, S. Mu, S. Liao, J. Zhang, X. Sun, An Isolated Zinc-Cobalt Atomic Pair for Highly Active and Durable Oxygen Reduction, Angew. Chem. Int. Ed., 58 (2019) 2622-2626.
[19] J. Li, M. Chen, D.A. Cullen, S. Hwang, M. Wang, B. Li, K. Liu, S. Karakalos, M. Lucero, H. Zhang, C. Lei, H. Xu, G.E. Sterbinsky, Z. Feng, D. Su, K.L. More, G. Wang, Z. Wang, G.

Wu, Atomically dispersed manganese catalysts for oxygen reduction in proton-exchange membrane fuel cells, Nat. Catal., 1 (2018) 935-945.
[20] M. Chen, Y. He, J.S. Spendelow, G. Wu, Atomically Dispersed Metal Catalysts for Oxygen Reduction, ACS Energy Lett., 4 (2019) 1619-1633.
[21] T. Al-Zoubi, Y. Zhou, X. Yin, B. Janicek, C. Sun, C.E. Schulz, X. Zhang, A.A. Gewirth, P. Huang, P. Zelenay, H. Yang, Preparation of Nonprecious Metal Electrocatalysts for the Reduction of Oxygen Using a Low-Temperature Sacrificial Metal, J. Am. Chem. Soc., 142 (2020) 5477-5481.
[22] X. Han, X. Ling, Y. Wang, T. Ma, C. Zhong, W. Hu, Y. Deng, Generation of Nanoparticle, Atomic-Cluster, and Single-Atom Cobalt Catalysts from Zeolitic Imidazole Frameworks by Spatial Isolation and Their Use in Zinc-Air Batteries, Angew. Chem. Int. Ed., 58 (2019) 5359-5364.
[23] Z. Chen, D. Zhao, C. Chen, Y. Xu, C. Sun, K. Zhao, M. Arif Khan, D. Ye, H. Zhao, J. Fang, X. Andy Sun, J. Zhang, Reconstruction of pH-universal atomic FeNC catalysts towards oxygen reduction reaction, J. Colloid Interface Sci., 582 (2021) 1033-1040.
[24] Z. Meng, S. Cai, R. Wang, H. Tang, S. Song, P. Tsiakaras, Bimetallic−organic framework-derived hierarchically porous Co-Zn-N-C as efficient catalyst for acidic oxygen reduction reaction, Appl. Catal. B: Environ., 244 (2019) 120-127.
[25] C. Tang, Y. Jiao, B. Shi, J.N. Liu, Z. Xie, X. Chen, Q. Zhang, S.Z. Qiao, Coordination Tunes Selectivity: Two-Electron Oxygen Reduction on High-Loading Molybdenum Single-Atom Catalysts, Angew. Chem. Int. Ed., 132 (2020) 9256-9261.
[26] W. Chen, J. Pei, C.T. He, J. Wan, H. Ren, Y. Zhu, Y. Wang, J. Dong, S. Tian, W.C. Cheong, S. Lu, L. Zheng, X. Zheng, W. Yan, Z. Zhuang, C. Chen, Q. Peng, D. Wang, Y. Li, Rational Design of Single Molybdenum Atoms Anchored on N-Doped Carbon for Effective Hydrogen Evolution Reaction, Angew. Chem. Int. Ed., 56 (2017) 16086-16090.
[27] L. Han, X. Liu, J. Chen, R. Lin, H. Liu, F. Lu, S. Bak, Z. Liang, S. Zhao, E. Stavitski, J. Luo, R.R. Adzic, H.L. Xin, Atomically Dispersed Molybdenum Catalysts for Efficient Ambient Nitrogen Fixation, Angew. Chem. Int. Ed., 58 (2019) 2321-2325.
[28] C. Wang, D. Wang, S. Liu, P. Jiang, Z. Lin, P. Xu, K. Yang, J. Lu, H. Tong, L. Hu, W. Zhang, Q. Chen, Engineering the coordination environment enables molybdenum single-atom catalyst for efficient oxygen reduction reaction, J. Catal., 389 (2020) 150-156.
[29] N. Cheng, L. Ren, X. Xu, Y. Du, S.X. Dou, Recent Development of Zeolitic Imidazolate Frameworks (ZIFs) Derived Porous Carbon Based Materials as Electrocatalysts, Adv. Energy Mater., 8 (2018) 1801257.
[30] S.S.A. Shah, T. Najam, M.K. Aslam, M. Ashfaq, M.M. Rahman, K. Wang, P. Tsiakaras, S. Song, Y. Wang, Recent advances on oxygen reduction electrocatalysis: Correlating the characteristic properties of metal organic frameworks and the derived nanomaterials, Appl. Catal. B: Environ., 268 (2020) 118570.
[31] A.-d. Tan, Y.-f. Wang, Z.-y. Fu, P. Tsiakaras, Z.-x. Liang, Highly effective oxygen reduction reaction electrocatalysis: Nitrogen-doped hierarchically mesoporous carbon derived from interpenetrated nonporous metal-organic frameworks, Appl. Catal. B: Environ., 218 (2017) 260-266.
[32] Y. Chen, Z. Li, Y. Zhu, D. Sun, X. Liu, L. Xu, Y. Tang, Atomic Fe Dispersed on N-Doped Carbon Hollow Nanospheres for High-Efficiency Electrocatalytic Oxygen Reduction, Adv. Mater., 31 (2019) e1806312.
[33] X. Li, J. Yu, M. Jaroniec, Hierarchical photocatalysts, Chem.Soc. Rev., 45 (2016) 2603-2636.
[34] G. Prieto, H. Tuysuz, N. Duyckaerts, J. Knossalla, G.H. Wang, F. Schuth, Hollow Nano- and Microstructures as Catalysts, Chem. Rev., 116 (2016) 14056-14119.
[35] S. Wang, Y. Wang, S.Q. Zang, X.W. Lou, Hierarchical Hollow Heterostructures for

Photocatalytic CO_2 Reduction and Water Splitting, Small Methods, 4 (2019) 1900586.
[36] F.X. Ma, H.B. Wu, B.Y. Xia, C.Y. Xu, X.W. Lou, Hierarchical beta-Mo_2C Nanotubes Organized by Ultrathin Nanosheets as a Highly Efficient Electrocatalyst for Hydrogen Production, Angew. Chem. Int. Ed., 54 (2015) 15395-15399.
[37] F.X. Ma, H. Hu, H.B. Wu, C.Y. Xu, Z. Xu, L. Zhen, X.W. David Lou, Formation of Uniform Fe_3O_4 Hollow Spheres Organized by Ultrathin Nanosheets and Their Excellent Lithium Storage Properties, Adv. Mater., 27 (2015) 4097-4101.
[38] F.-X. Ma, L. Yu, C.-Y. Xu, X.W. Lou, Self-supported formation of hierarchical $NiCo_2O_4$ tetragonal microtubes with enhanced electrochemical properties, Energy Environ. Sci., 9 (2016) 862-866.
[39] S. Wang, B.Y. Guan, Y. Lu, X.W.D. Lou, Formation of Hierarchical In_2S_3-$CdIn_2S_4$ Heterostructured Nanotubes for Efficient and Stable Visible Light CO_2 Reduction, J. Am. Chem. Soc., 139 (2017) 17305-17308.
[40] S. Chen, D.M. Koshy, Y. Tsao, R. Pfattner, X. Yan, D. Feng, Z. Bao, Highly Tunable and Facile Synthesis of Uniform Carbon Flower Particles, J. Am. Chem. Soc., 140 (2018) 10297-10304.
[41] T. Sugimoto;, Y. Wang;, H. Itoh;, A. Muramatsu, Systematic control of size, shape and internal structure of monodisperse α-Fe_2O_3 particles, Colloids Surf. A, 134 (1998) 265-279.
[42] Y. Yang, M. Luo, Y. Xing, S. Wang, W. Zhang, F. Lv, Y. Li, Y. Zhang, W. Wang, S. Guo, A Universal Strategy for Intimately Coupled Carbon Nanosheets/MoM Nanocrystals (M = P, S, C, and O) Hierarchical Hollow Nanospheres for Hydrogen Evolution Catalysis and Sodium-Ion Storage, Adv. Mater., 30 (2018) e1706085.
[43] J. Gao, Y. Wang, H. Wu, X. Liu, L. Wang, Q. Yu, A. Li, H. Wang, C. Song, Z. Gao, M. Peng, M. Zhang, N. Ma, J. Wang, W. Zhou, G. Wang, Z. Yin, D. Ma, Construction of a sp3/sp2 Carbon Interface in 3D N-Doped Nanocarbons for the Oxygen Reduction Reaction, Angew. Chem. Int. Ed., 58 (2019) 15089-15097.
[44] H. Jiang, J. Gu, X. Zheng, M. Liu, X. Qiu, L. Wang, W. Li, Z. Chen, X. Ji, J. Li, Defect-rich and ultrathin N doped carbon nanosheets as advanced trifunctional metal-free electrocatalysts for the ORR, OER and HER, Energy Environ. Sci., 12 (2019) 322-333.
[45] S.K. Singh, K. Takeyasu, J. Nakamura, Active Sites and Mechanism of Oxygen Reduction Reaction Electrocatalysis on Nitrogen-Doped Carbon Materials, Adv. Mater., 31 (2019) e1804297.
[46] M. Li, Y. Wang, Y. Zheng, G. Fu, D. Sun, Y. Li, Y. Tang, T. Ma, Gadolinium‐Induced Valence Structure Engineering for Enhanced Oxygen Electrocatalysis, Adv. Energy Mater., 10 (2020) 1903833.
[47] D. Yan, Y. Li, J. Huo, R. Chen, L. Dai, S. Wang, Defect Chemistry of Nonprecious-Metal Electrocatalysts for Oxygen Reactions, Adv. Mater., 29 (2017) 1606459.
[48] Y. Wang, G. Jia, X. Cui, X. Zhao, Q. Zhang, L. Gu, L. Zheng, L.H. Li, Q. Wu, D.J. Singh, D. Matsumura, T. Tsuji, Y.-T. Cui, J. Zhao, W. Zheng, Coordination Number Regulation of Molybdenum Single-Atom Nanozyme Peroxidase-like Specificity, Chem, 7 (2021) 436-449.
[49] Y. Wu, C. Ye, L. Yu, Y. Liu, J. Huang, J. Bi, L. Xue, J. Sun, J. Yang, W. Zhang, X. Wang, P. Xiong, J. Zhu, Soft template-directed interlayer confinement synthesis of a Fe-Co dual single-atom catalyst for Zn-air batteries, Energy Storage Mater., 45 (2022) 805-813.
[50] L. Zhang, J. Xiong, Y.-H. Qin, C.-W. Wang, Porous N–C catalyst synthesized by pyrolyzing g-C_3N_4 embedded in carbon as highly efficient oxygen reduction electrocatalysts for primary Zn-air battery, Carbon, 150 (2019) 475-484.
[51] H. Li, X. Shu, P. Tong, J. Zhang, P. An, Z. Lv, H. Tian, J. Zhang, H. Xia, Fe-Ni Alloy Nanoclusters Anchored on Carbon Aerogels as High-Efficiency Oxygen Electrocatalysts in Rechargeable Zn-Air Batteries, Small, 17 (2021) e2102002.
[52] H. Xu, D. Wang, P. Yang, L. Du, X. Lu, R. Li, L. Liu, J. Zhang, M. An, A hierarchically

porous Fe-N-C synthesized by dual melt-salt-mediated template as advanced electrocatalyst for efficient oxygen reduction in zinc-air battery, Appl. Catal. B: Environ., 305 (2022).
[53] J. Shi, X. Shu, C. Xiang, H. Li, Y. Li, W. Du, P. An, H. Tian, J. Zhang, H. Xia, Fe ultra-small particles anchored on carbon aerogels to enhance the oxygen reduction reaction in Zn-air batteries, J. Mater. Chem. A, 9 (2021) 6861-6871.
[54] P. Yu, L. Wang, F. Sun, Y. Xie, X. Liu, J. Ma, X. Wang, C. Tian, J. Li, H. Fu, Co Nanoislands Rooted on Co-N-C Nanosheets as Efficient Oxygen Electrocatalyst for Zn-Air Batteries, Adv. Mater., 31 (2019) e1901666.
[55] C. Li, H. Liu, Z. Yu, Novel and multifunctional inorganic mixing salt-templated 2D ultrathin Fe/Co-N/S-carbon nanosheets as effectively bifunctional electrocatalysts for Zn-air batteries, Appl. Catal. B: Environ., 241 (2019) 95-103.
[56] M. Zhang, E. Zhang, C. Hu, Y. Zhao, H.M. Zhang, Y. Zhang, M. Ji, J. Yu, G. Cong, H. Liu, J. Zhang, C. Zhu, J. Xu, Controlled Synthesis of Co@N-Doped Carbon by Pyrolysis of ZIF with 2-minobenzimidazole Ligand for Enhancing Oxygen Reduction Reaction and the Application in Zn-Air Battery, ACS Appl. Mater. Interface, 12 (2020) 11693-11701.
[57] X. Zhang, Z. Zhu, Y. Tan, K. Qin, F.X. Ma, J. Zhang, Co, Fe codoped holey carbon nanosheets as bifunctional oxygen electrocatalysts for rechargeable Zn-air batteries, Chem. Comm., 57 (2021) 2049-2052.